Supplementary material for "A frequency-optimised temperature record for the Holocene" by Essell et al. (2023) *Environmental Research Letters*

Materials and Methods

Temperature timeseries. Proxy timeseries used in production of our frequency-optimised record are found in the Temperature 12k database v.1.0.0, an extensive compilation of 1319 paleo-temperature timeseries from 679 sites [*1*]. Records are globally distributed (though their bias towards European and North American sites should be noted), span the past 12,000 years, and are composed of a variety of proxy types, making it preferable to earlier syntheses restricted to specific time horizons, proxy types, or geographical regions [*1*]. Records within the Temperature 12k database had to meet four key requirements for studying Holocene temperature variability: 1) they span at least 4,000 years during the Holocene, 2) they have a resolution finer than 400 years, 3) they have at least one age control every 3,000 years, and 4) they have a demonstrated relationship with temperature in the instrumental period [*1*]. We acknowledge issues in assuming a proxy-temperature from the instrumental period is valid throughout the Holocene, however, to date this is the most demonstrated means of palaeotemperature reconstruction. This is especially prevalent for proxies which have been found to be sensitive to more than one climatic variable (e.g., precipitation and temperature) and as such we excluded these in our production of our frequency-optimised record [*1*]. The Temperature 12k database is publicly available in Linked Paleo Data (LiPD) format at https://www.ncei.noaa.gov/access/paleo-search/study/27330. Proxy records from the LiPD datafile were imported to *R* v.4.1.0 [*2*] using the *readLipd* function in *lipdR* [*3*]. The Temperature 12k database is included within a much larger compilation of paleoclimate datasets stored under the LiPD framework. Records were selected to meet initial criteria [*1*] via *'In Compilation = 'Temp 12k'*.

For most sites in the Temperature 12k database, multiple timeseries are available, reflecting different proxy types, seasonal signals, or both. Avoiding signal duplication was necessary so not to inflate the temperature signal of a given record [*4*], therefore a subset containing 814 timeseries was used to produce our frequency-optimised record. All available proxy types were included, as proxy types differ in their preserved signals [*5*]. Annual mean temperature series were preferred, with those reflecting summer and winter temperature only being included in the absence of an annual mean series from the same proxy type. To select records meeting this criterion within the LiPD framework, series satisfying '*climateInterpretation1_seasonality = annual, summerOnly and winterOnly'* were extracted. On manual inspection, seven records were identified as seasonally mislabelled and corrected accordingly. Duplicate and temporally misaligned records were also corrected. Finally, a dataset of 814, globally distributed, albeit biased towards European and North American sites was produced (Fig. S1a, b). The dataset reflects a variety of archive types for the duration of the Holocene (Fig. S1c). The LiPD framework has a hierarchical structure and stores compilations of timeseries within nested lists [*6*]. To navigate this database and produce further subsets of timeseries differentiated by archive type, the *filter* function from the package *dplyr* [*7*] was used.

Many paleoclimate timeseries are associated with uneven sample spacing and chronological uncertainty, largely owing to slow accumulation rates which limit sample availability [*8*]. To place timeseries on a common timescale and to moderate the impacts of such uncertainty, timeseries were binned by averaging measurements within intervals corresponding to a given archive type's mean sampling resolution in the Holocene (Table S1). We deem these to be suitable bin intervals as age uncertainty is accounted for and the frequencies of variability a given archive type is capable of preserving are considered as this approach respects Nyquist frequency [*9*]. Kaufman et al. (2020) [*1*] employed a similar appraoch in their pairwise comparison composite. Finding limited difference in the composites produced using each of their five methodologies [*10*], this demonstrates appropriateness of the binning procedure employed.

To alleviate spatial differences in the magnitude of absolute temperature measurements while preserving temporal variability, the binned timeseries were normalised by conversion to Z-scores ($Z = (x-\bar{x})/\sigma$, where x is the observed value, $\bar{x}$ the timeseries mean and σ the timeseries standard deviation). This was performed in *R* v.4.1.0 using the *scale* function [*2*]. We appreciate as timeseries underlying our frequency-optimised record differ in length, normalising against their individual lengths could affect the presentation of the relative amplitude of temperature changes. There was, however, no common period for which all timeseries had datapoints. Statistical infilling procedures were deemed inappropriate as this would likely introduce artificial signals that would distort true climate signals we sought to identify and isolate. However, we demonstrate suitability of this normalisation by assessing the distribution of normalised temperature anomalies in each bin interval for each archive type (Fig. S2). Normalised timeseries for ice, midden, speleothem, and wood archives show little spread, while variability is greater in lacustrine, marine, and peat archives. Despite this, the distribution of anomalies remains small and any differences more likely reflect spatial differences in temperature variability [*11*] rather than artefacts of normalisation, demonstrating suitability of this normalisation procedure in this scenario. We encourage others to check for common overlap periods for which timeseries could be normalised against in future application of our methodology.

Temperature reconstruction. Holocene temperature as recorded in ice, lacustrine, marine, midden, peat, speleothem, and wood archives, was reconstructed using a bootstrap procedure (Fig. S3). This involves performing a finite number of re-sampling experiments to obtain a theoretical sample representative of both high and low order observations, enabling robust calculation of the statistical properties of a dataset when sufficient iterations are performed [*12*]. We considered it suitable for production of our archive-specific temperature histories as only those series with similar resolution were combined, thus smoothing effects are dampened. To calculate mean temperature for ice (n =28), lacustrine (n =367), marine (n =317), midden (n =10), peat (n =76), speleothem (n =13), and wood (n =3) archive subsets, a bootstrap procedure was applied to the normalised, binned timeseries. A total of 1,000 real number values were randomly drawn with replacement from series within a given archive-specific subset of proxy records for each bin interval in years between 0–12,000 years BP. Reconstructed temperature was taken as the mean of the values sampled in bin intervals ($\bar{x} = \Sigma x/n$, *where* Σx is sum of the observations, and n the number of observations, in this case 1,000). The 95% confidence intervals for each archive-specific temperature history were calculated for the normalised timeseries, prior to undergoing bootstrapping ($CI = \bar{x} \pm z(\sigma/\sqrt{n})$, where z is the confidence level value, in this case 1.960, and σ the sample standard deviation). No spatial gridding was applied in this procedure due to limited availability of proxy series in some, particularly Southern Hemisphere locations (Fig. S1a). We however acknowledge this invokes a spatial bias in our record and thus regard it to better reflect Northern Hemisphere temperatures, as the majority of the proxy archives derive from this locality [*1*].

Our frequency-optimised approach to multi-proxy reconstruction is based on nonlinear dynamical system theory, assuming the long-term behaviour of a system is ruled by sets of differential equations [*13*]. Signals were identified and isolated using methods demonstrated as appropriate in analysis of climate timeseries [*14*]. Two signal processing techniques form the basis of our frequency-optimised approach: spectral analysis and bandpass filtering. Spectral analysis provides a means of measuring the strength of periodic components in a timeseries [*15*]. Methods of spectral estimation traditionally derive from the principles of Fourier transform functions, whereby differential equations are used to decompose a timeseries into its frequency domain by characterising periodicities as sine and cosine functions [*16*]. The multi-taper method (MTM) of spectral analysis follows such principles [*17*], but additionally employs a tapered windowing approach to reduce endpoint discontinuities that contaminate spectral estimates with substantial low-frequency variability and alleviate variance-resolution trade-offs, thereby enabling identification of low-amplitude oscillations in relatively short series [*18*]. The ability to quantify the statistical significance of spectral density estimates is a further advantage of the MTM methodology [*18*]. The MTM analysis was performed in *R* v.4.1.0 using the *spec.mtm* function in the package *multi-taper v1.0-15* [*19*]. Spectral estimates are computed using a discrete prolate spheroidal sequences tapered window, centred using spheroidal sequences, the most nearly band-limited functions [*20*]. Bandpass filtering isolates the periodic components in a timeseries. A digital filter is used to pass, or preserve, frequencies within a specified spectral range, and attenuate frequencies outside the range, enabling isolation of the periodic components underlying a timeseries [*21*]. Filter windows are generally symmetrical around the mid-point of the filter width, but the degree of edge tapering varies. We use a Tukey window to produce a clean bandpass with minimal spectral leakage, achievable due to the presence of ripple control factors [*22*]. In *R* v.4.1.0, bandpass filtering was carried out using the *bandpass* function in the package *astrochron v1.0* [*23*], where we specified 25% of the data series to be subject to tapering.

Signal isolation. To identify the archive types most suitable in preserving climate variability at interannual (<10 years), multi-decadal (10–150 years), multi-centennial (150–1000 years), multi-millennial (1000–6000 years) and ultra-long (>6000 years) timescales, MTM spectral analysis was applied to archive-specific temperature histories. The number of periodicities identified as significant at the 95% confidence interval within interannual, multi-decadal, multi-centennial, multi-millennial, and ultra-long timescales (Fig. S4) were used to deduce which timescale of variability a given archive type best reflects. As stochastic noise represents a relatively small proportion of paleoclimate timeseries [*5*], cyclicities which respect Nyquist frequency [*9*] are assumed to reflect true climate signals. Additionally, our binning procedure is expected to have minimised noise in our archive-specific temperature histories, deeming signals to be true climate variations. This led to wood being identified as the most appropriate archive type at an interannual scale, speleothem archives at multi-decadal scales, ice and midden archives at multi-centennial scales, peat and marine archives multi-millennial scales, and lacustrine archives at ultra-long timescales.

Bandpass filtering was employed to isolate the multi-decadal variability preserved in the speleothem temperature history, the multi-centennial variability in the ice and midden temperature histories, the multi-millennial variability in the peat and marine temperature histories, and the ultra-long variability in the lacustrine temperature history.

Dendro-derived temperature reconstructions are often assumed to reflect an interannual signal due to band-width limits to dendrochronological records [*24,25*]. However, it is not unreasonable to assume there may be some low frequency signal in our wood temperature history due to the exceptionally long-length of the three dendro (i.e., tree-ring width) chronologies from which the wood temperature history is derived. We counter this effect by assuming any such low frequency trends to be linear, hence apply linear detrending in *R* v.4.1.0 using the *detrend* function in *astrochron* v1.0 [*23*]. It is assumed the signal remaining after linear detrending reflects an interannual signal. The wood temperature history is temporally limited to 7,450 years BP and as such, a synthetic series was generated to extend the coverage of the interannual signal from 7,451–12,000 years BP. This synthetic series resembles the variability of wood observations in the pre-industrial Common Era (0–1850 CE). The pre-industrial Common Era is a suitable training period as sample availability is highest, dating precise [*26*], and the divergence problem avoided [*27*]. Again, we applied linear detrending to remove any possible low frequency artefacts. An Autoregressive Integrated Moving Average (i.e., ARIMA) model was then fit to this detrended series to enable back casting and replication [*28,29*]. In *R* v.4.1.0, an ARIMA model was fit using the *auto.arima* function from *forecast* v8.15 [*30*], which employs the Hyndman-Khandakar algorithm to ensure a good fit between the model and observations [*30*]. The *simulate* function [*2*] was used to backcast the interannual fluctuations characteristic of the wood reconstruction beyond 7,450 years BP, however, only one iteration was produced as averaging many iterations would attenuate the randomly modelled interannual signal [*31*]. We acknowledge caveats of this approach, namely the assumption that the magnitude of high-frequency anomalies of the pre-industrial Common Era prevailed in the early Holocene. The early Holocene was characterised by starkly different ice sheet and vegetation extent, sea level, and insolation, inferring Earth's boundary conditions differed to the pre-industrial Common Era. It is uncertain whether associated effects of an increased meridional temperature gradients increased the magnitude of high-frequency climate fluctuations [*32*]. However, we use Earth system model simulations to demonstrate our approach appropriately represents interannual extremes in the early Holocene in the absence of dendro-derived temperature reconstructions for this period. Variance and standard deviation of the 10-year bandpass of mean annual Northern Hemisphere landmass temperature simulated by the CCSM3-TraCE-21k Earth system model simulation [*33*] does not significantly differ in the period that the synthetic portion of our frequency-optimised series covers (7,451–12,000 years BP) from that of the pre-industrial Common Era (0–1850 CE) (p =0.47 in f- and t-test). We used model simulations for Northern Hemisphere landmasses as our wood temperature history is biased towards this locality. On this basis, we argue the pre-industrial Common Era is a suitable training period from which to derive our synthetic portion of our interannual series due to similarity in the magnitude of high-frequency extremes in these periods. This is additionally supported by forcing reconstructions which show prevalence of volcanic eruptions during the early Holocene [*34*], which were also characteristic of the pre-industrial Common Era [*35*].

Frequency-optimised record. The sum of isolated signals reflecting interannual, multi-decadal, multi-centennial, multi-millennial, and ultra-long timescales (Fig. 2) was then calculated to generate our frequency-optimised record of Holocene temperature (Fig. 1). In case of multi-centennial and multi-millennial scales where multiple archive types best reflect these timescales of variability, the contribution of each band-passed signal was weighted by the number of archives used.

We acknowledge spatial biases in the timeseries underlying our frequency-optimised record, particularly at induvial archive scales (Fig. S1). However, due to environmental constraints on where proxy archives can accumulate, it is unfeasible to expect each archive type to be globally distributed. 455 of the 814 of the proxy records that underlie our record are located between 40° and 70°N in a circumpolar belt across Eurasia and North America and most of the biogeochemical archives are active in, or sensitive to warm season conditions [*1*]. We therefore deem our frequency-optimised record to better reflect Northern Hemisphere warm season temperatures. This is supported by the long-term trend of frequency-optimised record resembling that of simulated Northern Hemisphere summer temperatures (Fig. S7). If our approach is to be applied on a truly global scale, we encourage further acquisition of low- and high-resolution proxy-climate reconstructions from a wide geographical area and application of a spatial binning procedure to moderate the effects of uneven record distribution that will likely prevail.

Confidence intervals are deliberately permissive to account for non-climate variability preserved in proxy archives [*5*] and year-to-year uncertainty associated with annually resolved climate records. Confidence intervals were calculated by summing the 95% confidence intervals of the archive-temperature histories from which our record is derived (Fig. S3). In absence of an ability to produce of confidence intervals beyond 7,450 years BP for the wood series, two standard deviations from the mean of the synthetic interannual variability were used in its place.

Proxy-model comparison. We compared our frequency-optimised record to three transient Earth system model simulations. Comparisons were made in the frequency domain, computing the Morlet wavelets [*36*], in *MATLAB* R2021a using the *wt* command (Fig. 4), and MTM power spectra in *R* v.4.1.0 [*19*]. We carried out this analysis on our frequency-optimised record, existing multi-proxy reconstructions [*10,37-39*] and Northern Hemisphere summer (Figs. 4, S5), global annual (Figs. S5, S6), and Northern Hemisphere annual (Figs. S5, S7) model simulations [*33,40-43*]. MPI-ESM1.2 is a transient Earth system model simulation for the period 100–7,950 years BP [*40,41*]. In the model run considered here, the *slo0050* run, atmosphere, ocean and dynamic vegetation components are forced by prescribed variations in orbitally induced insolation, greenhouse gas concentrations, land-use change, volcanic aerosol distribution, solar irradiance, and stratospheric ozone distribution [*40,44*]. IPSL-TR6AV-Sr02 is a transient Earth system model simulation for the period 0–6,000 years BP [*42,43*]. This modified version of the IPSL-CM5A model [*45*] couples atmospheric, oceanic, sea-ice, ocean biogeochemical and dynamic global vegetation models to simulate the full range of global climate system dynamics. Vegetation and phenology components are interactive, while aerosol and solar radiation are accounted for by prescribing the optical distribution of dust, sea salt, sulphate, and particulate organic matter. CCSM3-TraCE-21k is a transient Earth system model simulation starting from the Last Glacial Maximum around 21,000 BP years BP and ending in 1990 CE [*33*]. Completed using the NCAR CCSM3 [*46*], this coupled atmosphere-ocean general circulation model includes a dynamic global vegetation model component, and is forced by orbital, greenhouse gases, ice sheet and meltwater forcing mechanisms; herein used over the period 12,000–0 years BP.

Figures (S1-S7)

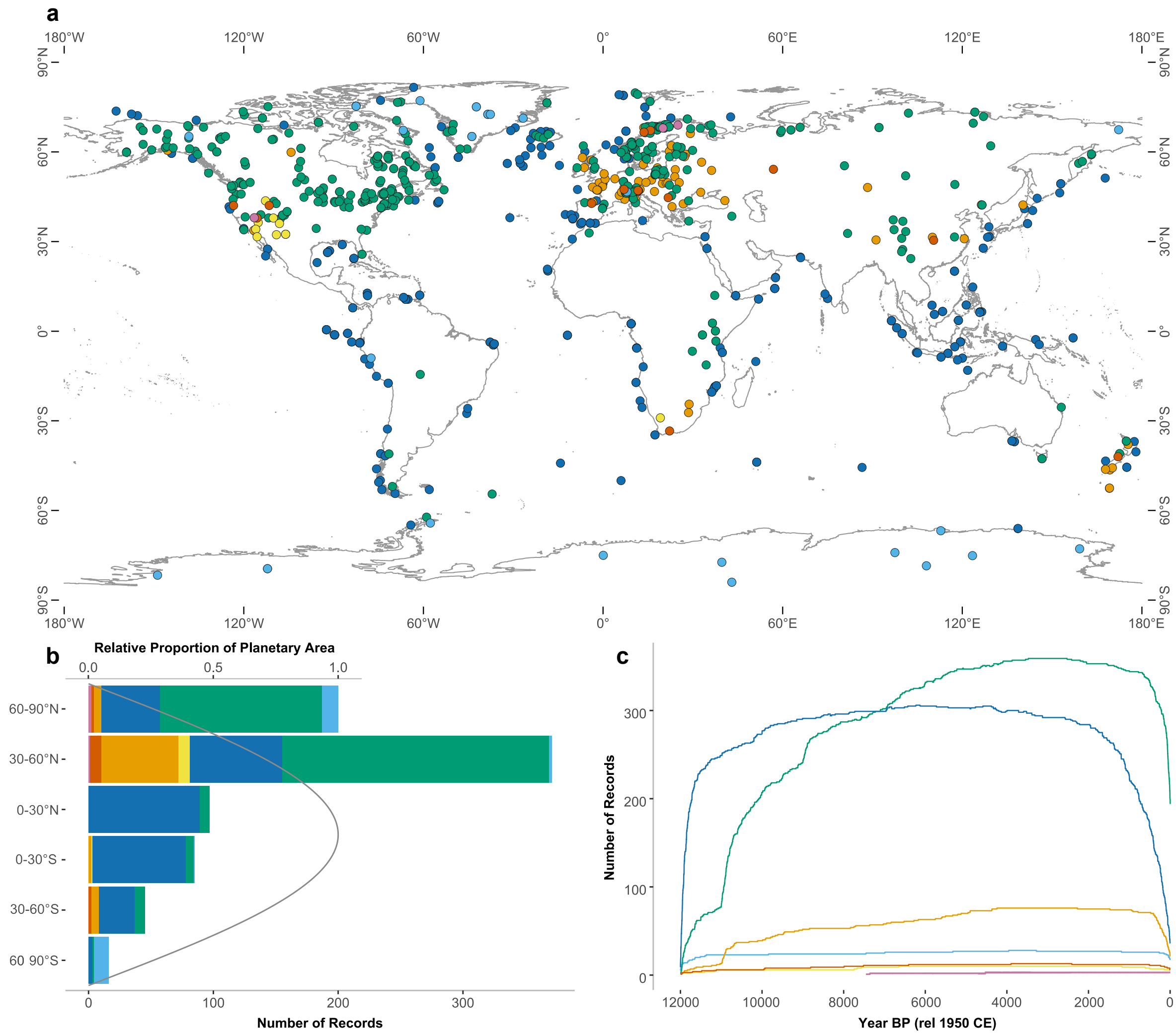

Fig. S1. Record distribution. Spatiotemporal distribution of the records in subset of the Temperature 12k database [*1*] used in this study (*n* =814). In (**a**), coloured circles show the geographical distribution of sites and archive type of each record. (**b**) Latitudinal distribution of sites, differentiated by archive type. (**c**) Number of records available for each archive type in time. In each panel, ice records are light blue, lacustrine green, marine dark blue, midden yellow, peat orange, speleothem red, and wood pink.

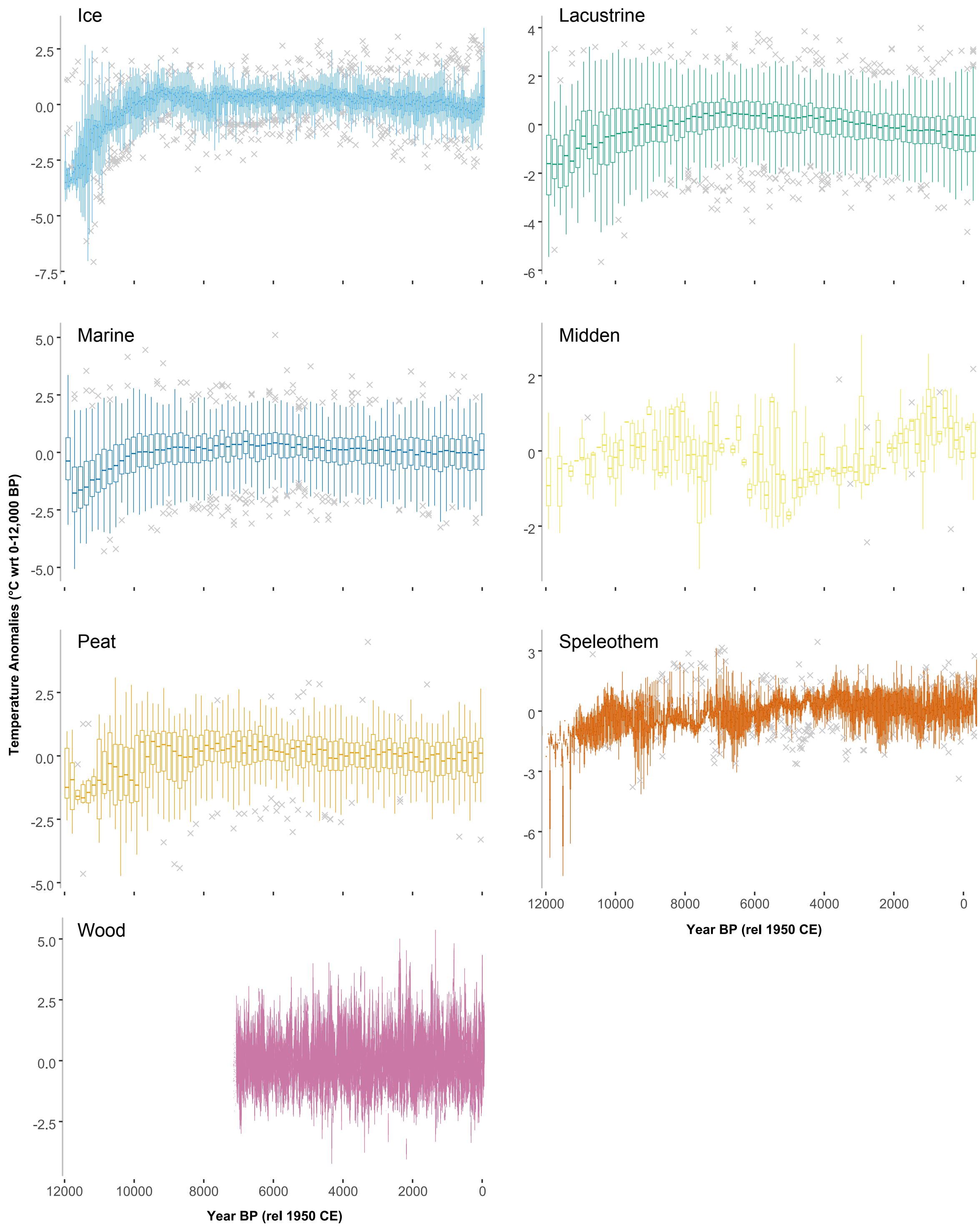

Fig. S2. Distribution of temperature anomalies. Boxplots showing the distribution of the normalised temperature anomalies in each bin interval for ice (light blue), lacustrine (green), marine (dark blue), midden (yellow), peat (orange), speleothem (red), and wood (pink) archives. Box shows the median, 25th and 75th quartiles. Whiskers show minimum and maximum values. Grey crosses show outliers.

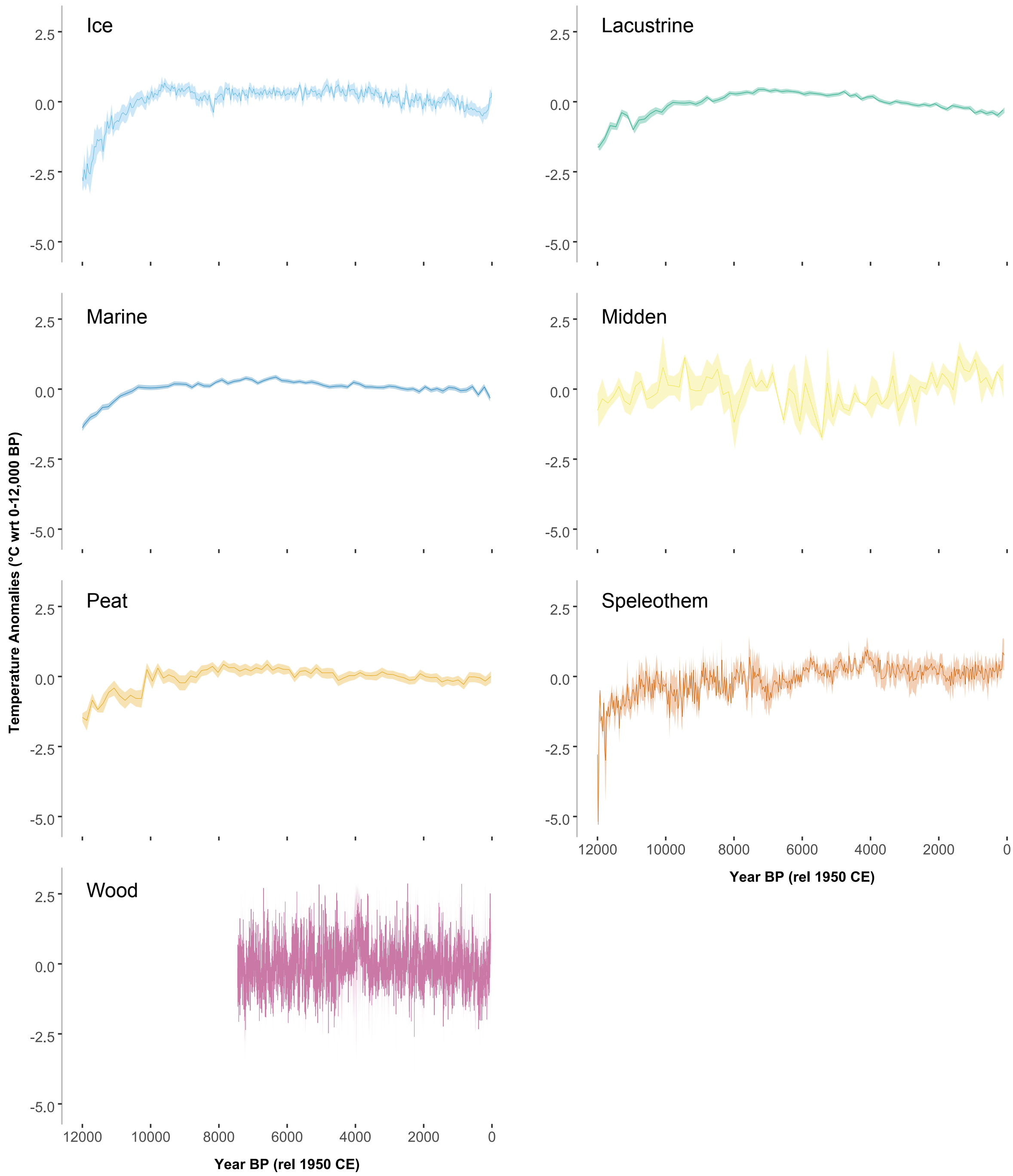

Fig. S3. Archive-specific temperature histories. Temperature histories for ice, lacustrine, marine, midden, peat, speleothem, and wood archives produced using the subset of records in the Temperature12k database [*1*] designated for use in this study. Temperature is reconstructed using a bootstrap procedure, using 1,000 iterations with replacement. Shading indicates 95% confidence intervals. Values are plotted as anomalies relative to the Holocene mean temperature.

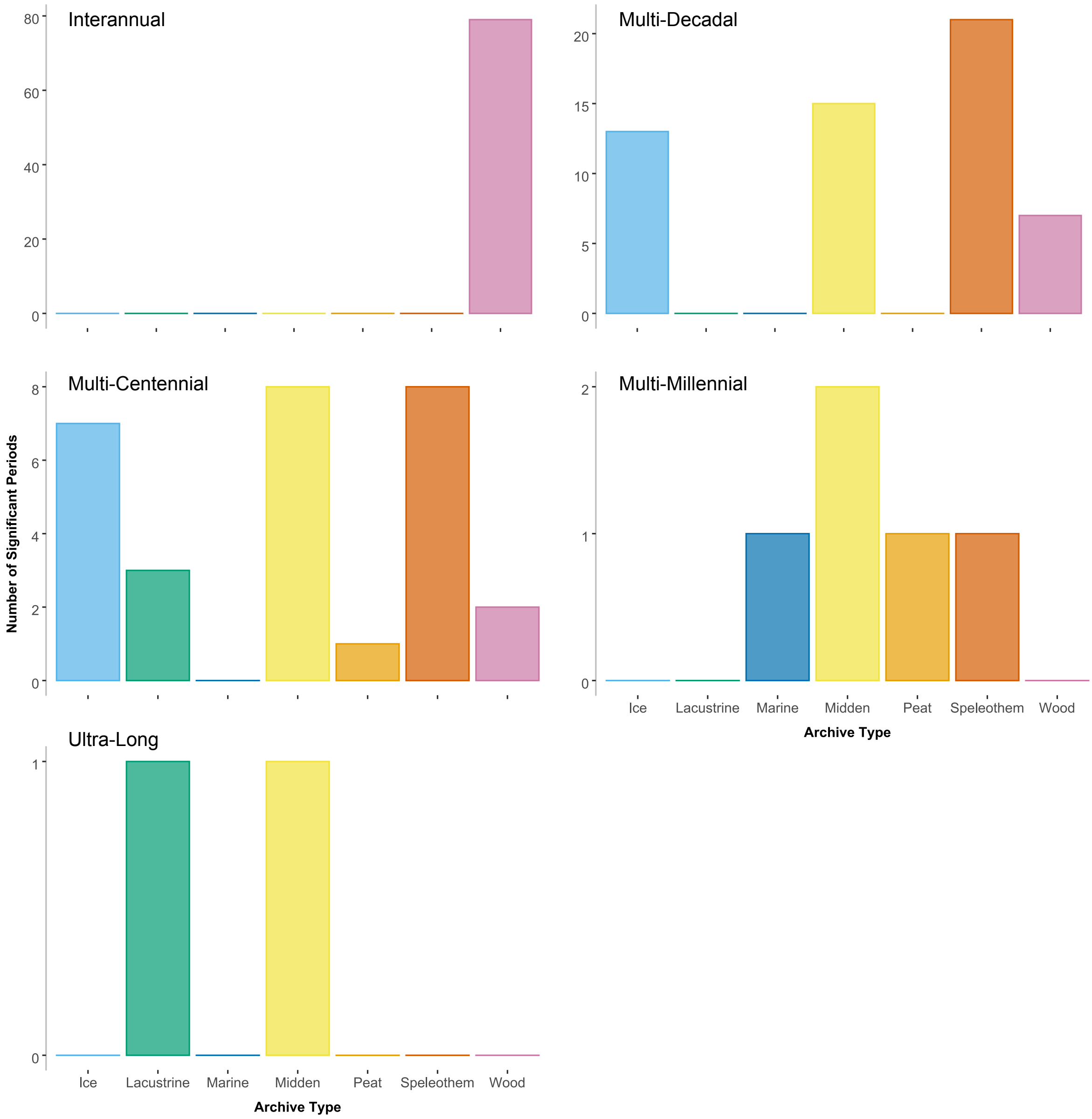

Fig. S4. Significant periodicities. Number of periods identified by MTM spectral analysis as significant at the 95% confidence interval at interannual (<10 years), multi-decadal (10–150 years), multi-centennial (150–1,000 years), multi-millennial (1,000–6,000 years) and ultra-long (>6,000 years) timescales for ice (light blue), lacustrine (green), marine (dark blue), midden (yellow), peat (orange), speleothem (red), and wood (pink) archives.

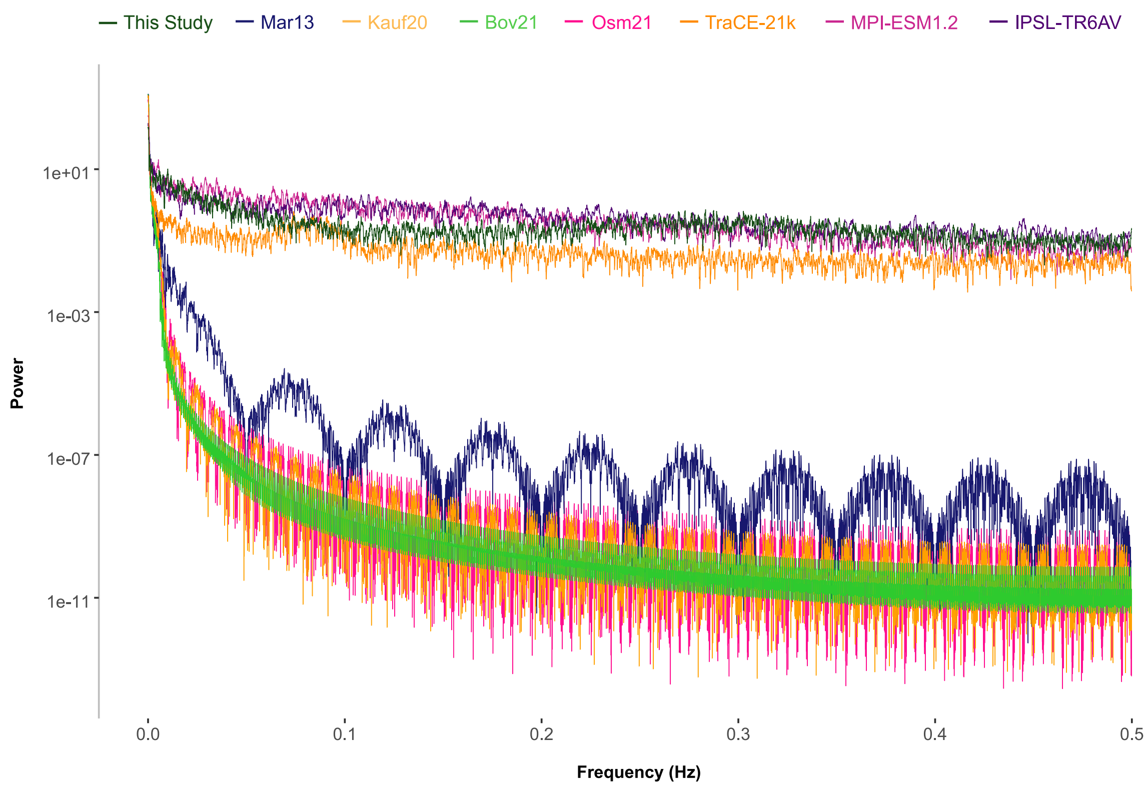

Fig. S5. Power spectra. Log power distribution of frequency components identified in: Marcott et al. (2013) GMST reconstruction [*37*], Kaufman et al. (2020) multi-method ensemble [*10*], Bova et al. (2021) seasonally unadjusted series [*38*], Osman et al. (2021) proxy-based series [*39*], our frequency-optimised record (This Study), and global annual mean surface temperature simulated using MPI-ESM1.2 [*40,41*], IPSL-TR6AV-Sr02 [*42,43*], and CCSM3-TraCE-21ka [*33*] transient Earth system models. Power spectra are computed using MTM spectral analysis for the period each record covers between 0–12,000 years BP.

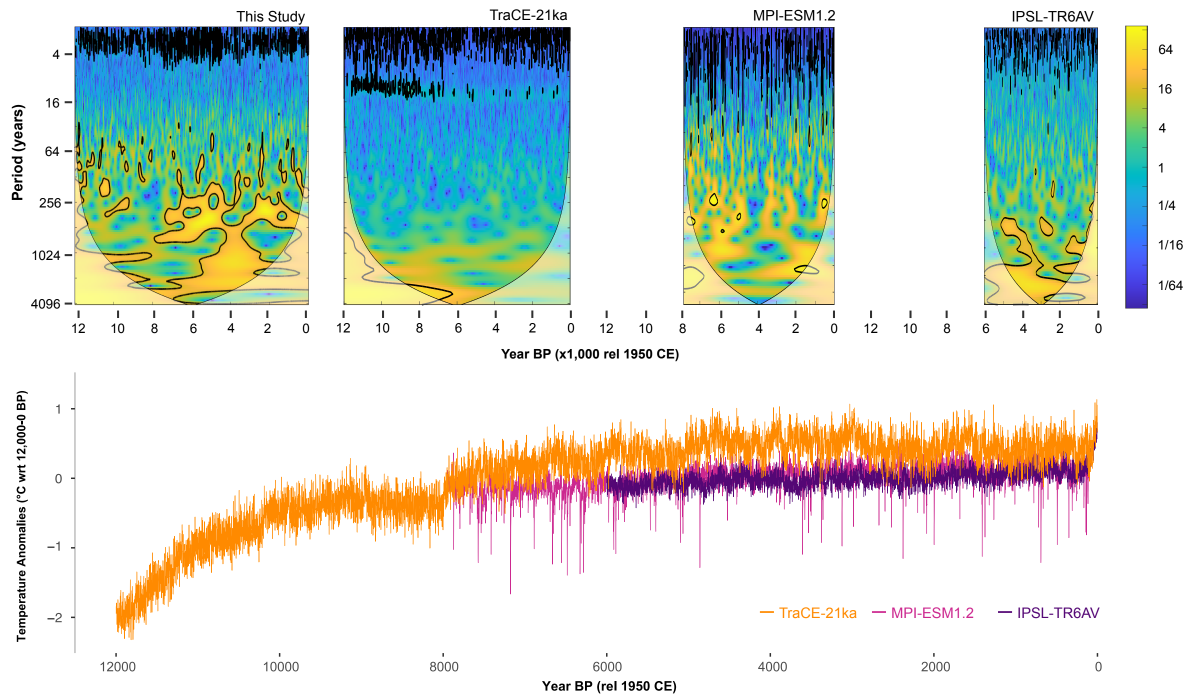

Fig. S6. Global annual temperature. Upper row shows wavelet power spectra of our frequency-optimised record and global annual mean temperature changes simulated using MPI-ESM1.2 [*40,41*], IPSL-TR6AV-Sr02 [*42,43*], and CCSM3-TraCE-21ka [*33*] transient Earth system models. Spectral signatures were calculated over the individual record lengths. Contours enclose periodicities significant at the 95% confidence interval, and shadings represent the cone of influence. Units reflect log spectral power. Bottom row shows the evolution of global annual mean temperature simulated using MPI-ESM1.2 [*40,41*], IPSL-TR6AV-Sr02 [*42,43*], and CCSM3-TraCE-21ka [*33*] transient Earth system models. Records are plotted relative to their Holocene mean (12,000–0 years BP).

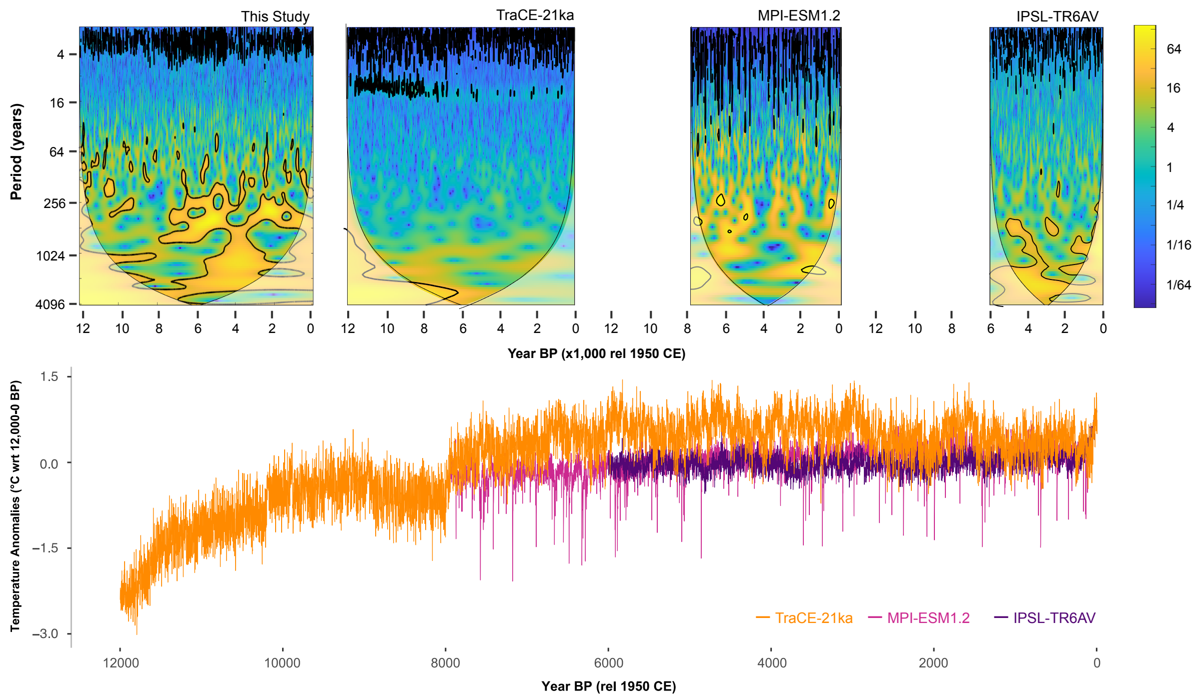

Fig. S7. Northern Hemisphere annual temperature. Upper row shows wavelet power spectra of our frequency-optimised record and Northern Hemisphere annual mean temperature changes simulated using MPI-ESM1.2 [*40,41*], IPSL-TR6AV-Sr02 [*42,43*], and CCSM3-TraCE-21ka [*33*] transient Earth system models. Spectral signatures were calculated over the individual record lengths. Contours enclose periodicities significant at the 95% confidence interval, and shadings represent the cone of influence. Units reflect log spectral power. Bottom row shows the evolution of Northern Hemisphere annual mean temperature simulated by using MPI-ESM1.2 [*40,41*], IPSL-TR6AV-Sr02 [*42,43*], and CCSM3-TraCE-21ka [*33*] transient Earth system models. Records are plotted relative to their Holocene mean (12,000–0 years BP).

Tables (S1)

Table S1. Proxy-temperature records. Types and characteristics of proxy archives in the subset of Temperature 12k database [*1*] records used in construction of our frequency-optimised temperature record (*n* =814).

Archive Type	Number of records	Mean resolution (years)	Median resolution (years)	Standard deviation of resolution (years)	Minimum sample age (year BP)	Maximum sample age (year BP)	Proxies	
Ice	28	42	20	49	0	12000	• Borehole depth • Bubble frequency • $\delta^{18}O$ • δD	• Gas • Hybrid • Isotope diffusion • Melt layer
Lake	367	168	158	98	0	12000	• Alkenone • BSi • Chironomid • Chlorophyll • $\delta^{18}O$ • Diatom • GDGT	• Hybrid • Mg/Ca • Particle size • Pollen • TOC
Marine	317	175	134	140	0	12000	• Alkenone • $\delta^{18}O$ • Diatom • Dinocyst • Foraminifera • GDGT	• Long chain diol • Mg/Ca • Pollen • Radiolaria
Midden	10	162	139	99	0	12000	• Macrofossil • Pollen	
Peat	76	160	145	94	0	12000	• C_{15} fatty alcohols • Chironomid • $\delta^{13}C$	• $\delta^{18}O$ • GDGT • Pollen
Speleothem	13	27	25	28	0	12000	• 3-OH fatty acids • $\delta^{13}C$	• $\delta^{18}O$ • δD
Wood	3	1	1	0	0	7450	• Tree-ring width	

References (SI)

1. Kaufman, D., McKay, N., Routson, C., Erb, M., Davis, B., Heiri, O., Jaccard, S., Tierney, J., Dätwyler, C., Axford, Y., Brussel, T., Cartapanis, O., Chase, B., Dawson, A., de Vernal, A., Engels, S., Jonkers, L., Marsicek, J., Moffa-Sánchez, P., Morrill, C., Orsi, A., Rehfeld, K., Saunders, K., Sommer, P. S., Thomas, E., Tonello, M., Tóth, M., Vachula, R., Andreev, A., Bertrand, S., Biskaborn, B., Bringué, M., Brooks, S., Caniupán, M., Chevalier, M., Cwynar, L., Emile-Geay, J., Fegyveresi, J., Feurdean, A., Finsinger, W., Fortin, M. C., Foster, L., Fox, M., Gajewski, K., Grosjean, M., Hausmann, S., Heinrichs, M., Holmes, N., Ilyashuk, B., Ilyashuk, E., Juggins, S., Khider, D., Koinig, K., Langdon, P., Larocque-Tobler, I., Li, J., Lotter, A., Luoto, T., Mackay, A., Magyari, E., Malevich, S., Mark, B., Massaferro, J., Montade, V., Nazarova, L., Novenko, E., Pařil, P., Pearson, E., Peros, M., Pienitz, R., Płóciennik, M., Porinchu, D., Potito, A., Rees, A., Reinemann, S., Roberts, S., Rolland, N., Salonen, S., Self, A., Seppä, H., Shala, S., St-Jacques, J. M., Stenni, B., Syrykh, L., Tarrats, P., Taylor, K., van den Bos, V., Velle, G., Wahl, E., Walker, I., Wilmshurst, J., Zhang, E. & Zhilich, S. A global database of Holocene paleotemperature records. *Sci. Data* **7**, 1–34 (2020).
2. R Core Team R. A language and environment for statistical computing. R Foundation for Statistical Computing. https://www.R-project.org/ (2021).
3. Heiser, C. & McKay, N. lipdR: LiPD utilities for R. https://www.lipd.net (2015).
4. Bradley, R.S. & Jones, P. D. 'Little Ice Age' summer temperature variations; their nature and relevance to recent global warming trends. *Holocene* **3**, 367–376 (1993).
5. Meyers, S. R., Sageman, B. B. & Pagani, M. Resolving Milankovitch: Consideration of signal and noise. *Ameri. J. Sci.* **308**, 770–786 (2008).
6. McKay, N. P. & Emile-Geay, J. Technical note: The Linked Paleo Data framework - A common tongue for paleoclimatology. *Clim. Past* **12**, 1093–1100 (2016).

7. Wickham, H., François, r., Henry, L. & Müller, K. dplyr: A Grammar of Data Manipulation. R package version 1.0.8. https://CRAN.R-project.org/package=dplyr (2022).
8. Yiou, P., Baert, E. & Loutre, M. F. Spectral analysis of climate data. Surveys Geophys. 17, 619–663 (1996).
9. Nyquist, H. Certain Topics in Telegraph Transmission Theory. *Trans. Ameri. Inst. Electrical Engin.* **47**, 617–644 (1928).
10. Kaufman, D., McKay, N., Routson, C., Erb, M., Dätwyler, C., Sommer, P. S., Heiri, O. & Davis, B. Holocene global mean surface temperature, a multi-method reconstruction approach. *Sci. Data* **7**, 201 (2020).
11. Bader, J., Jungclaus, J., Krivova, N., Lorenz, S., Maycock, A., Raddatz, T., Schmidt, H., Toohey, M., Wu, C. J. & Claussen, M. Global temperature modes shed light on the Holocene temperature conundrum. *Nat. Comm.* **11**, 4726 (2020).
12. Metropolis, N. & Ulam, S. The Monte Carlo Method. *J. Ameri. Stat. Assoc.* **44**, 335–341 (1949).
13. Bergé, P., Pomeau, Y. & Vidal, C. L'ordre dans le chaos: vers une approche déterministe de la turbulence. Hermann, Paris. (1988).
14. Ghil, M., Kimoto, M. & Neelin, J. D. Nonlinear Dynamics and Predictability in the Atmospheric Sciences. *Rev. Geophys.* **29**, 46–55 (1991).
15. Jenkins, G. M. & Watts, D. G. Spectral Analysis and Its Applications. Holden-Day. (1968).
16. Fourier, J. B. J. Théorie Analytique de la Chaleur. Firmin Didot, Paris (1822).
17. Thomson, D. J. Spectrum estimation and harmonic analysis. *Proc. IEEE* **70**, 1055–1096 (1982).
18. Mann, M. E. & Lees, J. M. Robust estimation of background noise and signal detection in climatic time series. *Clim. Change* **33**, 409–445 (1996).

19. Rahim, K. Applications of Multitaper Spectral Analysis to Nonstationary Data. Queens's University, Kingston, Ontario, Canada (2014).
20. Thomson, D. J. Time series analysis of Holocene climate data. *Philosophical Transactions of the Royal Society of London. Series A, Mathematical and Physical Sciences* **330**, 601–616 (1990).
21. Menke, W. & Menke, J. Detecting correlations among data. In: Environmental Data Analysis with MatLab. Academic Press, Amsterdam. 167–201 (2012).
22. Roy, T. K. & Morshed, M. Performance analysis of low pass FIR filters design using Kaiser, Gaussian and Tukey window function methods. In: Proceedings of 2013 2nd International Conference on Advances in Electrical Engineering. ICAEE, Dhaka. 1–6 (2013).
23. Meyers, S. R. Astrochron: An R Package for Astrochronology. https://cran.r-project.org/package=astrochron%0A (2014).
24. Cook, E. R., Briffa, K. R., Meko, D. M., Graybill, D. A., & Funkhouser, G. The 'segment length curse' in long tree-ring chronology development for palaeoclimatic studies. *Holocene* **5**, 229–237 (1995).
25. Esper, J., Frank, D. C., Timonen, M., Zorita, E., Wilson, R. J. S., Luterbacher, J., Holzkämper, S., Fischer, N., Wagner, S., Nievergelt, D., Verstege, A. & Büntgen, U. Orbital forcing of tree-ring data. *Nat. Clim. Change* **2**, 862–866 (2012).
26. Esper, J. & Büntgen, U. The future of paleoclimate. *Clim. Res.* **83**, 57–59 (2021).
27. D'Arrigo, R., Wilson, R., Liepert, B. & Cherubini, P. On the 'Divergence Problem' in Northern Forests: A review of the tree-ring evidence and possible causes. *Glob. Plan. Change* **60**, 289–305 (2008).
28. Akaike, H. Fitting autoregressive models for prediction. *Ann. Inst. Stat. Mathematics* **21**, 243–247 (1969).

29. Box, G. E. P. & Jenkins, G. M. Time Series Analysis: Forecasting and Control. Holden-Day, San Francisco (1970).

30. Hyndman, R. R. J. & Khandakar, Y. Automatic Time Series Forecasting: The forecast Package for R. *J. Stat. Software* **26**, 1–22 (2008).

31. North, G. R., Kim, K. Y., Shen, S. S. P. & Hardin, J. W. Detection of forced climate signals. Part I: filter theory. *J. Clim.* **8**, 401–408 (1995).

32. Rehfeld, K., Münch, T., Ho, S. & Laepple, T. Global patterns of declining temperature variability from the Last Glacial Maximum to the Holocene. *Nature* **554**, 356–359 (2018).

33. Liu, Z., Otto-Bliesner, B. L., He, F., Brady. E. C., Tomas, R., Clark, P. U., Carlson, A. E., Lynch-Stieglitz, J., Curry, W., Brook, E., Erickson, D., Jacob, R., Kutzbach, J. & Cheng, J. Transient Simulation of Last Deglaciation with a New Mechanism for Bølling-Allerød Warming. *Science* **325**, 310–314 (2009).

34. Sigl, M., Toohey, M., McConnell. J., R., Cole-Dai, J. & Severi, M. Volcanic stratospheric sulfur injections and aerosol optical depth during the Holocene (past 11 500 years) from a bipolar ice-core array. *Earth Syst. Sci. Data* **14**, 3167–3196 (2022).

35. Büntgen, U., Arseneault, D., Boucher, É., Churakova (Sidorova), O. V., Gennaretti, F., Crivellaro, A., Hughes, M. K., Kirdyanov, A. V., Klippel, L., Krusic, P. J., Linderholm, H. W., Ljungqvist, F. C., Ludescher, J., McCormick, M., Myglan, V. S., Nicolussi, K., Piermattei, A., Oppenheimer, C., Reinig, F., Sigl, M., Vaganov, E. A. & Esper, J. Prominent role of volcanism in Common Era climate variability and human history. *Dendrochronologia* **64**, 125757 (2020).

36. Grinsted, A. Cross wavelet and wavelet coherence. https://github.com/Grinsted/wavelet-coherence (2021).

37. Marcott, S. A., Shakun, J. D., Clark, P. U. & Mix, A. C. A Reconstruction of Regional and Global Temperature for the Past 11,300 Years. *Science* **339**, 1198–1201 (2013).

38. Bova, S., Rosenthal, Y., Liu, Z., Godad, S. P. & Yan, M. Seasonal origin of the thermal maxima at the Holocene and the last interglacial. *Nature* **589**, 548–553 (2021).
39. Osman, M. B., Tierney, J. E., Zhu, J., Tardif, R., Hakim, G. J., King, J. & Poulsen C. J. Globally resolved surface temperatures since the Last Glacial Maximum. *Nature* **599**, 239–244 (2021).
40. Bader, J., Jungclaus, J., Krivova, N., Lorenz, S., Maycock, A., Raddatz, T., Schmidt, H., Toohey, M., Wu, C. J. & Claussen, M. Global temperature modes shed light on the Holocene temperature conundrum. *Nat. Comm.* **11**, 4726 (2020).
41. Dallmeyer, A., Claussen, M., Lorenz, S. J., Sigl, M., Toohey, M. & Herzschuh, U. Holocene vegetation transitions and their climatic drivers in MPI-ESM1.2. *Clim. Past* **17**, 2481–2513 (2021).
42. Braconnot, P., Zhu, D., Marti, O. & Servonnat, J. Strengths and challenges for transient Mid- to Late Holocene simulations with dynamical vegetation. *Clim. Past* **15**, 997–1024 (2019).
43. Braconnot, P., Crétat, J., Marti, O., Balkanski, Y., Caubel, A., Cozic, A., Foujols, M.-A., & Sanogo, S.: Impact of Multiscale Variability on Last 6,000 Years Indian and West African Monsoon Rain. *Geophys. Res. Let.* **46**, 14021–14029 (2019).
44. Mauritsen, T., Bader, J., Becker, T., Behrens, J., Bittner, M., Brokopf, R., Brovkin, V., Claussen, M., Crueger, T., Esch, M., Fast, I., Fiedler, S., Fläschner, D., Gayler, V., Giorgetta, M., Goll, D. S., Haak, H., Hagemann, S., Hedemann, C., Hohenegger, C., Ilyina, T., Jahns, T., Jimenéz-de-la-Cuesta, D., Jungclaus, J., Kleinen, T., Kloster, S., Kracher, D., Kinne, S., Kleberg, D., Lasslop, G., Kornblueh, L., Marotzke, J., Matei, D., Meraner, K., Mikolajewicz, U., Modali, K., Möbis, B., Müller, W. A., Nabel, J. E. M. S., Nam, C. C. W., Notz, D., Nyawira, S. S., Paulsen, H., Peters, K., Pincus, R., Pohlmann, H., Pongratz, J., Popp, M., Raddatz, T. J., Rast, S., Redler, R., Reick, C. H., Rohrschneider, T., Schemann,

V., Schmidt, H., Schnur, R., Schulzweida, U., Six, K. D., Stein, L., Stemmler, I., Stevens, B., von Storch, J. S., Tian, F., Voigt, A., Vrese, P., Wieners, K. H., Wilkenskjeld, S., Winkler, A. & Roeckner, E. Developments in the MPI-M Earth System Model version 1.2 (MPI-ESM1.2) and Its Response to Increasing CO_2. *J. Adv. Modeling Earth Syst.* **11**, 998–1038 (2019).

45. Dufresne, J. L., Foujols, M. A., Denvil, S., Caubel, A., Marti, O., Aumont, O., Balkanski, Y., Bekki, S., Bellenger, H., Benshila, R., Bony, S., Bopp, L., Braconnot, P., Brockmann, P., Cadule, P., Cheruy, F., Codron, F., Cozic, A., Cugnet, D., de Noblet, N., Duvel, J. P., Ethé, C., Fairhead, L., Fichefet, T., Flavoni, S., Friedlingstein, P., Grandpeix, J. Y., Guez, L., Guilyardi, E., Hauglustaine, D., Hourdin, F., Idelkadi, A., Ghattas, J., Joussaume, S., Kageyama, M., Krinner, G., Labetoulle, S., Lahellec, A., Lefebvre, M. P., Lefevre, F., Levy, C., Li, Z. X., Lloyd, J., Lott, F., Madec, G., Mancip, M., Marchand, M., Masson, S., Meurdesoif, Y., Mignot, J., Musat, I., Parouty, S., Polcher, J., Rio, C., Schulz, M., Swingedouw, D., Szopa, S., Talandier, C., Terray, P., Viovy, N. & Vuichard, N. Climate change projections using the IPSL-CM5 Earth System Model: From CMIP3 to CMIP5. *Clim. Dyn.* **40**, 2123–2165 (2013).

46. Collins, W. D., Bitz, C. M., Blackmon, M. L., Bonan, G. B., Bretherton, C. S., Carton, J. A., Chang, P., Doney, S. C., Hack, J. J., Henderson, T. B., Kiehl, J. T., Large, W. G., McKenna, D. S., Santer, B. D. & Smith, R. D. The Community Climate System Model version 3 (CCSM3). *J. Clim.* **19**, 2122–2143 (2006).

Code availability

The R code that implements the frequency-optimised method will be available from the authors upon request.